Nanoscale

PAPER

View Article Online
View Journal | View Issue

Cite this: *Nanoscale*, 2018, **10**, 8728

Hierarchical TiN nanoparticles-assembled nanopillars for flexible supercapacitors with high volumetric capacitance†

Ping Qin,‡[a] Xingxing Li,‡[a] Biao Gao,*[a] Jijiang Fu,[a] Lu Xia,[a] Xuming Zhang,*[a] Kaifu Huo,[b] Wenli Shen[c] and Paul K. Chu[d]

Received 21st February 2018,
Accepted 12th April 2018

DOI: 10.1039/c8nr01485j

rsc.li/nanoscale

Titanium nitride (TiN) is an attractive electrode material in fast charging/discharging supercapacitors because of its excellent conductivity. However, the low capacitance and mechanical brittleness of TiN restricts its further application in flexible supercapacitors with high energy density. Thus, it is still a challenge to rationally design TiN electrodes with both high electrochemical and mechanical properties. Herein, the hierarchical TiN nanoparticles-assembled nanopillars (H-TiN NPs) array as binder free electrodes were obtained by nitriding of hierarchical titanium dioxide (TiO_2) nanopillars, which was produced by a simple hydrothermal treatment of anodic TiO_2 nanotubes (NTs) array in water. The porous TiN nanoparticles connected to each other to form ordered nanopillar arrays, effectively providing larger specific surface area and more active sites for charge storage. The H-TiN NPs delivered a high volumetric capacitance of 120 F cm^{-3} at 0.83 A cm^{-3}, which is better than that of TiN NTs arrays (69 F cm^{-3} at 0.83 A cm^{-3}). After assembling into all-solid-state devices, the H-TiN NPs based supercapacitors exhibited outstanding volumetric capacitance of 5.9 F cm^{-3} at 0.02 A cm^{-3} and a high energy density of 0.53 mW h cm^{-3}. Our results reveal a new strategy to optimize the supercapacitive performance of metal nitrides.

Introduction

Owing to the rapid consumption of fossil fuels, environmental pollution and global warming, which are considered as hazards impacting economic development, renewable energy technologies are effective in solving all the above cited problems.[1,2] Energy storage systems including supercapacitors (SCs) and lithium ion batteries are the primary storage devices to store intermittent energy and SCs have attracted much attention due to the high power density, short charge storage time and long life-span.[2] On the basis of the intrinsic charge storage property, SCs could be divided into electrochemical double-layer capacitors (EDLCs) and pseudocapacitors.[3] EDLCs store charge *via* ions absorbed/desorbed on the interface of electrode and electrolyte, while pseudocapacitors store charge through Faraday reactions across the electrode and electrolyte interface.[4] The typical EDLCs electrode materials include carbon nanotubes (CNTs), graphene and activated carbon, which usually have large surface area and high conductivity, but possess poor capacitance. In contrast, pseudocapacitive materials including transition metal oxides (TMOs)[5–7] and conducting polymers[8,9] could provide larger specific pseudocapacitance than carbon materials.[10] Nevertheless, the low conductivity of TMOs and the unsatisfactory stability of conducting polymers usually hinder their further application for high performance SCs.[11]

Highly conductive transition metal nitrides such as TiN,[12,13] Mo_2N,[14] VN,[15] MoN[16] and Nb_4N_5 [17,18] have emerged as supercapacitive electrodes for SCs in view of their high capacitance of the order of 100–1340 F g^{-1}. Among them, TiN possesses an ultrahigh conductivity of 4.5 × 10^6 S m^{-1}, which is close to that of pure metals.[19,20] Thus, various TiN nanostructures usually work as substrates to support other redox active materials such as MnO_2, MoO_x, polyaniline, and polypyrrole for higher rate capability and active material utilization.[21,22] Improving intrinsic capacitance of TiN nanoarchitecture is another way to make them available for fast char-

[a]*The State Key Laboratory of Refractories and Metallurgy, Institute of Advanced Materials and Nanotechnology, Wuhan University of Science and Technology, Wuhan 430081, China. E-mail: gaobiao@wust.edu.cn, xumzhang@wust.edu.cn*
[b]*Wuhan National Laboratory for Optoelectronics (WNLO), School of Optical and Electronic Information Huazhong University of Science and Technology Wuhan 430074, China*
[c]*Department of Physics, Arizona State University, Tempe 85281, USA*
[d]*Department of Physics and Department of Materials Science and Engineering, City University of Hong Kong, Tat Chee Avenue, Kowloon, Hong Kong, China*

†Electronic supplementary information (ESI) available: SEM for H-TiO_2 NPs; SEM, BET and XPS for H-TiN NPs; electrochemical characterizations for H-TiN NPs. See DOI: 10.1039/c8nr01485j

‡These authors contributed equally to this work.

ging/discharging SCs or flexible SCs. For example, Choi *et al.* decreased the particle sizes of TiN to 8.23 nm to acquire a high gravimetric capacitance of 238 F g^{-1}.[23] However, nano-sized TiN powders are usually deposited on a current collector by mixing the inactive adhesion binder and conductive carbon black, resulting in additional interfacial resistance and unnecessary weight increase.[24,25] Compared to the electrodes fabricated by slurry coating methods, self-supported electrodes render higher active material utilization and enhanced structural integrity due to their free non-active binding and conducting property.[26] Moreover, freestanding electrodes with considerable flexibility have great potential for flexible energy storage devices. Thus, self-supported and flexible electrodes have been paid intensive attention.[27] Depositing active materials on flexible fibers/textiles is an effective and widely reported method to fabricate freestanding electrodes. For example, Lu *et al.* and Xie *et al.* grew TiN nanowires on a carbon cloth to obtain free-standing and flexible electrodes for bendable supercapacitors.[28,29] In our recent study, nanoporous TiN nanotubes (NTs) array fabricated by anodic processing of a Ti foil and further annealing in NH_3 atmosphere delivered a considerable area capacitance of 83 mF cm^{-2} (0.2 mA cm^{-2}).[21] Different from growing nanostructures on a carbon cloth, the direct fabrication of TiN NTs on bendable Ti foil is expected to bode better adhesion and decreased interfacial resistance. Unfortunately, compared to other metal nitride electrodes, the electrochemical performance of the TiN NTs electrode remains to be improved to satisfy practical demands.

Herein, we report hierarchical TiN nanoparticles assembled in nanopillars (H-TiN NPs) array consisting of alternatively stacked and connected TiN nanoparticles by directly nitriding hierarchical TiO_2 nanopillars (H-TiO_2 NPs) array, which was obtained by anodization of Ti foil and subsequent hydrothermal treatment in deionized water (DW). The self-supported and binder-free H-TiN NPs electrode endows the following advantages for flexible SCs. First, porous H-TiN NPs with large surface area could provide more active sites and facile electrolyte penetration channels to improve utilization of the electrode material. Second, TiN nanoparticles connecting each other to form ordered nanopillar arrays could effectively decrease interfacial resistance between the nanoparticles. Third, H-TiN NPs grown on flexible Ti foil electrode have good flexibility. As a consequence, the H-TiN NPs electrode possesses high volumetric capacitance (120 F cm^{-3}), which is larger than that of TiN NTs (69 F cm^{-3}) at a current density of 0.83 A cm^{-3}. The flexible all-solid-state symmetric device composed of two H-TiN NPs electrodes has high volumetric capacitance of 5.9 F cm^{-3} and energy density of 0.53 mW h cm^{-3} at a current density of 0.02 A cm^{-3}. Moreover, the flexible SCs exhibit outstanding cycling stability with capacitance retention of 99% after 3000 cycles and a superb rate capability owing to the high conductivity of the H-TiN NPs electrode. The well-defined H-TiN NPs with increased capacitance can be produced without complex steps and this strategy could be extended to prepare other TMNs.

Experimental

Synthesis of H-TiN NPs

Titanium foil (99.9% pure, Aldrich), anhydrous alcohol (AR, Sigma-Aldrich), ammonium fluoride (AR, Sigma-Aldrich), anhydrous methanol (AR, Sigma-Aldrich), ethylene glycol (AR, Sigma-Aldrich), and polyvinyl alcohol (PVA, AR, 1799, Sigma-Aldrich) were used without purification. The titanium foil (1 × 2 × 0.01 cm^3) was polished with sandpaper and rinsed with a mixture of DW and ethanol (1 : 1) ultrasonically for 10 min to remove surface impurities. The TiO_2 NTs were prepared by anodization method on direct current power (IT6834, ITECH)[30] in a two electrode system with the Ti foil as the working electrode and graphite plate as the counter electrode. Anodization was conducted at 60 V for 1 h at 25 °C with a mixed electrolyte containing ethylene glycol (90 vol%), ammonium fluoride (0.5 wt%), H_2O (5 vol%) and methanol (5 vol%). After rinsing with DW to remove the residual electrolyte, the as-obtained TiO_2 NTs were dried and put in a Teflon-lined stainless-steel autoclave with DW. The vessel was heated to 100 °C for 12 h. Subsequently, the hydrothermal products were annealed in air at 500 °C for 1 h to obtain the H-TiO_2 NPs. The H-TiN NPs were obtained by thermal treatment of H-TiO_2 NPs in NH_3 at 800 °C for 3 h. The TiN NTs were produced in the similar way, but without the hydrothermal treatment step. The areal mass loading of electrode film was 1.2–1.4 mg cm^{-2}.

Materials characterization

X-ray diffraction with Cu K_α radiation (λ = 1.5418 Å, XRD, Philips X' Pert Pro), field-emission scanning electron microscopy (FESEM, FEI Nova 450 Nano), high-resolution transmission electron microscopy (HR-TEM, FEI Titan G2 60-300), X-ray photoelectron spectroscopy (XPS, Thermo Scientific Escalab 250Xi) and nitrogen adsorption/desorption (Micromeritics, ASAP 2020 analyzer) were performed to analyze the fine composition and porous characteristics of the samples. The pore size distributions were obtained by the Barrett–Joyner–Halenda (BJH) model with the sample mass of 100 mg.

Electrochemical characterization

The electrochemical studies were performed using an electrochemical workstation (CHI 760e) with a three-electrode system. TiN NTs and H-TiN NPs acted as working electrodes with carbon plate as the counter electrode and the saturated calomel electrode (SCE) as the reference electrode in 1 M H_2SO_4 solution under the potential window of 0–0.8 V. The flexible all-solid-state devices were prepared by assembling two H-TiN NPs (1 × 2 cm^2) with the PVA based gel. The gel electrolyte was prepared by mixing commercial PVA powder (3 g) and concentrated H_2SO_4 (3 g) in 30 mL of DW under vigorous stirring at 85 °C. Before assembly, the H-TiN NPs electrodes were put into the H_2SO_4/PVA gel and soaked for 10–20 min. The H-TiN NPs based device was obtained by overlapping two electrodes face-to-face and solidifying overnight. The areal and

volumetric capacitances were calculated by galvanostatic charging/discharging (GCD) based on eqn (1) and (2):

$$C_s = \frac{I \times \Delta t}{\Delta V \times S}, \quad (1)$$

$$C_v = \frac{C_s}{d}, \quad (2)$$

where C_s (F cm^{-2}) and C_v (F cm^{-3}) are the areal and volumetric specific capacitance, respectively, ΔV (V) is the potential window, S (cm^2) is the area of the TiN electrode, I (A) is charging/discharging current density, Δt (s) is the discharge time and d (cm) is the thickness of the H-TiN NPs array. The energy density (E, W h cm^{-3}) and power density (P, W cm^{-3}) were calculated by eqn (3) and (4) as follows:

$$E = \frac{1}{2 \times 3600} C_v \Delta V^2, \quad (3)$$

$$P = \frac{E}{\Delta t}. \quad (4)$$

Results and discussion

The synthesis of the self-supported and binder-free H-TiN NPs electrode is illustrated in Fig. 1 and the TiO_2 NTs are fabricated on the Ti foil by anodization method. Fig. S1a and b† depict the SEM images of TiO_2 NTs with vertical alignment on Ti foil with uniform inner diameter of 100–150 nm and a wall thickness of 20 nm. After the hydrothermal treatment, the H-TiN NPs have the same diameter as the TiO_2 NTs (Fig. S1c and d†). During hydrothermal process, the amorphous TiO_2 NTs in water are easily dissolved, forming insoluble species of $Ti(OH)_6^{2-}$. Then, this species is dehydrated and deposited simultaneously to form H-TiO_2 NPs.[5] The reaction involving transformation of TiO_2 NTs to H-TiO_2 NPs could be described by the following equations:

$$TiO_x + 4H_2O + (1 - x/2)O_2 = Ti(OH)_6^{2-} + 2H^+ \ (1 < x < 2) \text{ and}$$

$$Ti(OH)_6^{2-} + 2H^+ = TiO_2 + 4H_2O$$

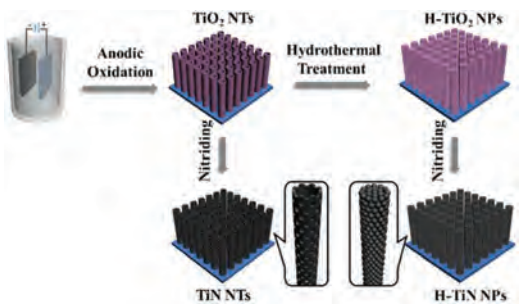

Fig. 1 Schematic illustration of the formation process of TiN NTs and H-TiN NPs.

The newly generated TiO_2 nanoparticles are nucleated and grown on the inter surface of amorphous TiO_2 NTs wall, resulting in the nanoparticles connecting each other until the NTs disappear.

The TiO_2 NTs and H-TiO_2 NPs are thermally treated in air and then in NH_3 to obtain the TiN NTs and H-TiN NPs, respectively. The top-view SEM images of the TiN NTs and H-TiN NPs in Fig. 2a and d show that the TiN NTs have tubular morphology and the corresponding side-view SEM images in Fig. 2b and e disclose that the NTs and NPs are vertically aligned with similar diameter of about 100–150 nm and height of 6 μm. The high-resolution SEM images (insets in Fig. 2b and e) show that the H-TiN NPs are coarser than the TiN NTs because of the nanopillars consisting of nanoparticles with a size of 10–25 nm, as confirmed by TEM image (Fig. 2f). The high-resolution TEM (HR-TEM) images shown in the insets of Fig. 2c and f imply that TiN NTs and H-TiN NPs show lattice fringe spacing of 0.209 and 0.243 nm corresponding to the plane of (200) and (111) of cubic TiN, respectively.

The XRD patterns of the H-TiO_2 NPs and H-TiN NPs are shown in Fig. 3a. The bottom diffraction peaks of the anodic product are attributed to the anatase phase of TiO_2 (JCPDS No. 02-0387)[25] except the peaks at 40, 53, 63 and 70.7°, originating from the Ti substrate. After nitridation, new peaks at 36.8, 42.8, 62.1, 74.4 and 78.3° belong to (111), (200), (220), (311) and (222) planes of cubic TiN (JCPDS No. 65-5774),[28] respectively, which is consistent with HR-TEM (inset in Fig. 2f). The fine XPS of Ti 2p spectra acquired from the H-TiN NPs and H-TiO_2 NPs are displayed in Fig. 3b. Three chemical states of Ti 2p are detected from the H-TiN NPs, including Ti–O bond (Ti $2p_{3/2}$, 458.5 eV; Ti $2p_{1/2}$, 464.2 eV), Ti–N–O bond (Ti $2p_{3/2}$, 456.8 eV; Ti $2p_{1/2}$, 462.4 eV), and Ti–N bond (Ti $2p_{3/2}$, 455.6 eV; Ti $2p_{1/2}$, 461.3 eV).[24,31] In contrast, there is only one pair of Ti–O peaks emerged in H-TiO_2 NPs, further verifying that the product is TiN. Moreover, the N 1s spectrum of H-TiN NPs (Fig. S2†) shows two peaks at 396.7 and 397.4 eV associated

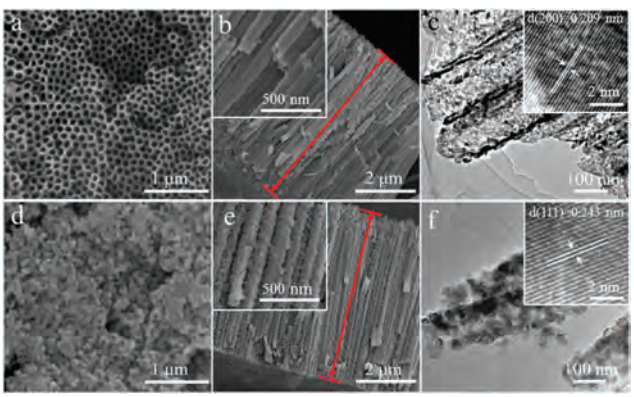

Fig. 2 Top-view SEM images of (a) TiN NTs and (d) H-TiN NPs; side-view SEM images of (b) the TiN NTs and (e) H-TiN NPs. The insets in (b) and (e) are the high-resolution SEM; TEM images of (c) the TiN NTs and (f) H-TiN NPs. The insets in (c) and (f) are the high-resolution TEM.

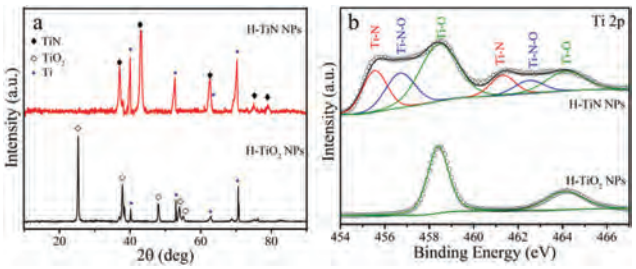

Fig. 3 (a) XRD patterns of the H-TiN NPs and H-TiO_2 NPs; (b) XPS of Ti 2p of H-TiN NPs and H-TiO_2 NPs.

with Ti–N and Ti–N–O of TiN, respectively, which is consistent with the Ti 2p spectrum.[31] Another peak at higher binding energy can be ascribed to the absorbed nitrogen.[31] The adsorption–desorption isotherms (Fig. S3†) of H-TiN NPs show typical hysteresis loop at high relative pressure range, indicating mesoporous characteristics, which result from the stacking of TiN nanoparticles. The Brunne–Emmet–Teller (BET) surface of H-TiN NPs (23.1 $m^2\ g^{-1}$) is about twice that of the TiN NTs (13.8 $m^2\ g^{-1}$). The BJH pore distribution of the TiN NTs show two main pore contributions. Larger pores with the size of 10–30 nm are attributed to the mesoporous structures of the stacked TiN nanoparticles, while the smaller pores of 2–5 nm confirm that the TiN nanoparticles are porous. The H-TiN NPs with increased BET specific surface and hierarchical pore distribution are supposed to offer more active sites for charge storage than that of TiN NTs.

The electrochemical performance of the samples was investigated by CV and GCD measurements. CV curves (Fig. 4a) of the H-TiN NPs and TiN NTs electrodes exhibit a closely rectangular shape at a scanning rate of 100 mV s^{-1} in 1 M H_2SO_4, indicating good capacitance. The integral surface of CV curve

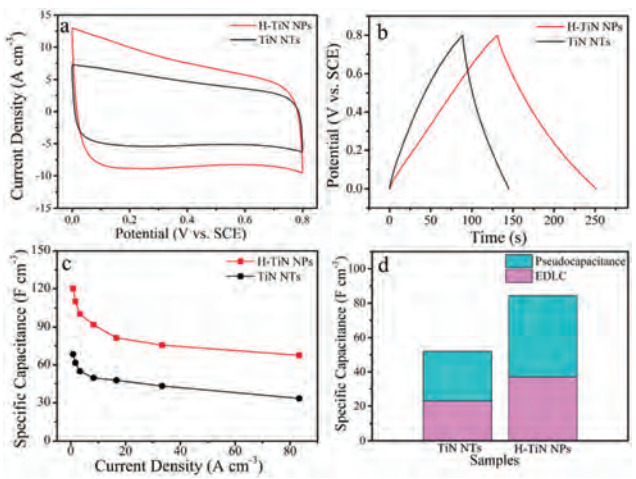

Fig. 4 Electrochemical performances of H-TiN NPs and TiN NTs electrodes: (a) CV curves at 100 mV s^{-1}; (b) GCD curves at 0.83 A cm^{-3}; (c) rate performance; (d) the contribution of EDLC and pseudocapacitance at a current density of 0.83 A cm^{-3} in 0.1 M H_2SO_4, 0.1 M HBF_4, 0.1 M $[(C_2H_5)_4N]_2SO_4$ and 0.1 M $[(C_2H_5)_4N]BF_4$.

detected from the H-TiN NPs is almost 1.5-times that of TiN NTs, depicting higher capacitance of H-TiN NPs. Furthermore, the CV curves of the H-TiN NPs at large scan rates of 200 mV s^{-1} retain their rectangular shape, implying fast charge transfer kinetics and good supercapacitive behavior (Fig. S4†). The GCD curves (Fig. 4b and S5†) of H-TiN NPs are symmetric triangular in shape and possess a high volumetric capacitance of 120 F cm^{-3} at a current density of 0.83 A cm^{-3}, which is larger than that of the porous TiN NTs (69 F cm^{-3}). The electrochemical impedance spectroscopy (EIS) data in Fig. S6a† shows that H-TiN NPs discloses an ultrasmall equivalent impedance of 0.2–0.3 Ω and exhibits rapid response with a diminutive characteristic time constant (τ) of 25.5 ms. τ is calculated by the equation of $\tau = 1/2\pi f$, where f is the characteristic frequency for a phase angle of −45° and π is the circular constant (Fig. S6b†).[32] The ultrasmall equivalent impedance and the fast responsive speed forebode high conductivity of the H-TiN NPs. In addition, the EIS spectrum of the TiN NTs is similar to that of the H-TiN NPs due to the outstanding conductivity of the TiN (Fig. S7†). Furthermore, the H-TiN NPs show higher volumetric capacitances than those of TiN NTs at all current densities from 0.83 to 83 A cm^{-3} (Fig. 4c). The corresponding area capacitance data of H-TiN NPs from 0.5 to 50 mA cm^{-2} are shown in Fig. S8.† The H-TiN NPs can still maintain a large volumetric capacitance (67 F cm^{-3}) even at a high current density of 83 A cm^{-3}, indicating the excellent rate capacitance due to the outstanding conductivity and convenient electrolyte transport channel. These results strongly suggest that the H-TiN NPs possess great potential for instantaneous energy delivery devices.

To evaluate the mechanism responsible for the higher capacitance, the electrochemical behavior of the TiN NTs and H-TiN NPs were measured in different electrolytes by the ion separation method.[33] The GCD curves of the TiN NTs and H-TiN NPs are acquired in 0.1 M H_2SO_4, 0.1 M HBF_4, 0.1 M $[(C_2H_5)_4N]_2SO_4$ and 0.1 M $[(C_2H_5)_4N]BF_4$ at a current density of 0.83 A cm^{-3} (Fig. S9†). Since $(C_2H_5)_4N^+$ and BF_4^- are regarded as inactive ions,[33] the H^+ and SO_4^{2-} ions could be isolated by $(C_2H_5)_4N^+$ and BF_4^-, respectively. The specific capacitances of the TiN NTs and H-TiN NPs are calculated by eqn (1) and (2). Both of them show a similar electrochemical behavior in H_2SO_4 and HBF_4, but the capacitances are larger than those in $[(C_2H_5)_4N]_2SO_4$ and $[(C_2H_5)_4N]BF_4$. The capacitance of TiN NTs and H-TiN NPs in $[(C_2H_5)_4N]_2SO_4$ and $[(C_2H_5)_4N]BF_4$ are attributed to the electrochemical double-layer capacitance (EDLC) from absorption/desorption of ions on the surface of TiN NTs and H-TiN NPs,[33] while the larger capacitance of the TiN NTs and H-TiN NPs in H_2SO_4 and HBF_4 can be ascribed to the pseudocapacitive reaction.[28] Fig. 4d depicts the statistics of the EDLC and pseudocapacitance obtained from the GCD curves of the H-TiN NPs and TiN NTs (Fig. S9†). The EDLC of the H-TiN NPs (37 F cm^{-3}) is 1.61-times larger than that of the TiN NTs (23 F cm^{-3}), which is attributable to the increase in BET surface area of H-TiN NPs compared to that of the TiN NTs, as indicated in the BET results (Fig. S3†).[34] Moreover, the calculated pseudocapacitance of the H-TiN NPs (47 F cm^{-3}) is also

larger than that of TiN NTs (29 F cm^{-3}) because of more exposed active sites of H-TiN NPs (57 mF cm^{-2}) than that of TiN NTs (26 mF cm^{-2}) (Fig. S10†).[35] The electrochemical active surface area can be measured by slope value of current density-scan rate line obtained from the CV curves at different scan rates (shown in Fig. S4†).[36] Moreover, the H-TiN NPs show excellent capacity retention of 94.3% after 3000 cycles at a scanning rate of 200 mV s^{-1} (Fig. S11†).

All-solid-state SCs were constructed symmetrically with the H-TiN NPs as electrodes and H_2SO_4/PVA gel as electrolytes. The electrochemical measurements were carried out in the potential range from 0 to 0.8 V. The volume of the cell containing the two electrodes and PVA/H_2SO_4 gel electrolyte was about 0.01 cm^3 (1 cm × 2 cm × 0.005 cm). The CV curves (Fig. 5a) of the device with a nearly rectangular shape at various scan rates depicts good capacitive behaviour. The GCD curves (Fig. 5b) show that the volumetric capacitance is calculated to be 5.9 and 4.8 F cm^{-3} at a current density of 0.02 and 0.2 A cm^{-3}, endowing a capacitance retention of 80% when the current density is increased 10 times. The volumetric capacitance of the H-TiN NPs is larger than that of the TiN nanowires/nanotubes grown on fibers/textiles.[28,31] Energy density (E) and power density (P) are two significant parameters for SCs application and can be determined from the Ragone plots. Fig. 5c shows the energy-power characteristics of the SCs, disclosing a high energy density of 0.53 mW h cm^{-3} on the basis of a considerable power density (0.08 W cm^{-3}) at 0.02 A cm^{-3}. Our results are better than those reported previously, including those obtained for SWCNTs based SCs (0.02 mW h cm^{-3} and 0.02 W cm^{-3}),[37] TiO_2@C based SCs (0.011 mW h cm^{-3} and 0.019 W cm^{-3}),[38] V_2O_3/N-rGO based SCs (0.55 mW h cm^{-3} and 0.035 W cm^{-3}),[39] GaN NW based SCs (0.25 mW h cm^{-3} and 0.02 W cm^{-3}),[40] sulfur-doped V_6O_{13-x} NWs based SCs (0.87 mW h cm^{-3} and 0.009 W cm^{-3}),[41] H-ZnO NW based SCs

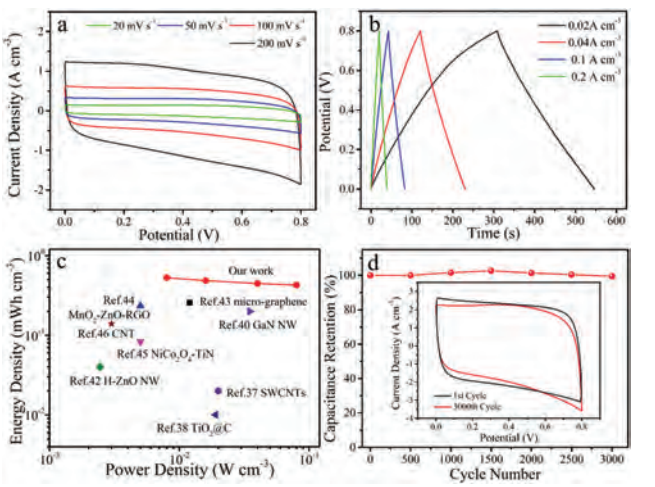

Fig. 5 All-solid-state SCs device based on H-TiN NPs: (a) CV curves; (b) GCD plots; (c) Ragone plot; (d) cycling stability of H-TiN NPs tested at 500 mV s^{-1}, the insert picture is the CV curves of the initial and after 3000 cycles.

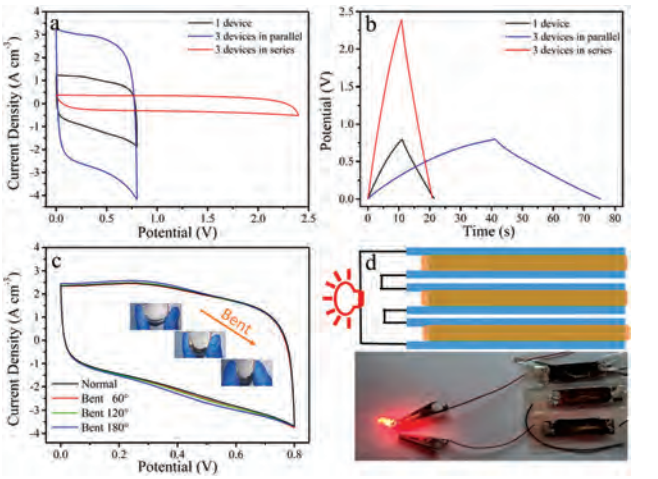

Fig. 6 (a) CV curves at 200 mV s^{-1} and (b) GCD plots of one single and three-equipped H-TiN NPs base SCs at a constant current density of 0.4 A cm^{-3}; (c) CV curves of bent state with different angle at 500 mV s^{-1}; (d) schematic illustration and digital picture of a red LED lighted by three SCs in series.

(0.04 mW h cm^{-3} and 0.002 W cm^{-3}),[42] micro-graphene based SCs (0.15 mW h cm^{-3} and 0.012 W cm^{-3}),[43] MnO_2-ZnO-RGO based SCs (0.234 mW h cm^{-3} and 0.005 W cm^{-3}),[44] $NiCo_2O_4$-TiN based SCs (0.083 mW h cm^{-3} and 0.005 W cm^{-3}),[45] as well as CNTs based SCs (0.14 mW h cm^{-3} and 0.003 W cm^{-3}).[46] Moreover, the flexible SCs based on H-TiN NPs have robust stability with 99% retention after 3000 cycles and the cycling CV curve is the same as the initial CV curve (Fig. 5d).

To further testify the function of the flexible SCs, three identical devices were connected in parallel circuit and series circuit. The three devices (defined as 1, 2 and 3) with same size of 1 × 2 × 0.005 cm^3 were tested by CV and GCD method. As shown in Fig. 6a, the total potential of the three units in series is 2.4 V, which is triple that of the single device. Moreover, the capacitance of the three devices in parallel is three times that of the single device (Fig. 6b). Interestingly, the CV curves of H-TiN NPs based device exhibit no evident attenuation even at different bent angles, as shown in Fig. 6c, foreboding remarkable flexibility and mechanical integrity. Moreover, a red light-emitting diode (LED) can be illuminated by the three devices in series, demonstrating that the H-TiN NPs can be a potential energy storage device in the near future (Fig. 6d).

Conclusions

Self-supporting and binder free H-TiN NPs electrodes were prepared by electrochemical anodization of Ti foil, hydrothermal treatment in pure water, and further annealing in ammonia. More active sites were exposed to electrolyte due to the increased surface area of the H-TiN NPs array assembled by connected TiN nanoparticles. The H-TiN NPs show higher

volumetric capacitance (120 F cm^{-3}) than TiN NTs (69 F cm^{-3}). All-solid-state SCs assembled by the H-TiN NPs electrodes possess an excellent volumetric capacitance of 5.9 F cm^{-3} at 0.02 A cm^{-3}, a high energy density of 0.53 mW h cm^{-3} as well as excellent stability. The simple fabrication strategy for the 1D inter-connected nanoparticles architecture is a new route to produce high-performance transition metal nitride electrodes.

Conflicts of interest

There are no conflicts to declare.

Acknowledgements

This study was financially supported by National Natural Science Foundation of China (51504171, 51572100 and 31500783), Outstanding Young and Middle-aged Scientific Innovation Team of Colleges and Universities of Hubei Province (T201402), the Opening Project of State Key Laboratory of High Performance Ceramics and Superfine Microstructure, Shanghai Institute of Ceramics, Chinese Academy of Sciences (SKL201609SIC), Project of Natural Science Foundation of Hubei Province (2015CFA116), City University of Hong Kong Strategic Research Grant (SRG) No. 7004644, and City University of Hong Kong Applied Research Grant (ARG) No. 9667122.

Notes and references

1 G. Yu, X. Xie, L. Pan, Z. Bao and Y. Cui, *Nano Energy*, 2013, **2**, 213.
2 A. González, E. Goikolea, J. A. Barrena and R. Mysyk, *Renewable Sustainable Energy Rev.*, 2016, **58**, 1189.
3 X. Li, S. Ding, X. Xiao, J. Shao, J. Wei, H. Pang and Y. Yu, *J. Mater. Chem. A*, 2017, **5**, 12774.
4 B. Li, P. Gu, Y. Feng, G. Zhang, K. Huang, H. Xue and H. Pang, *Adv. Funct. Mater.*, 2017, **27**, 1605784.
5 K. Huo, H. Wang, X. Zhang, Y. Cao and P. K. Chu, *ChemPlusChem*, 2012, **77**, 323.
6 X. Xiao, H. Song, S. Lin, Y. Zhou, X. Zhan, Z. Hu, Q. Zhang, J. Sun, B. Yang, T. Li, L. Jiao, J. Zhou, J. Tang and Y. Gogotsi, *Nat. Commun.*, 2016, **7**, 11296.
7 Z. Hu, X. Xiao, H. Jin, T. Li, M. Chen, Z. Liang, Z. Guo, J. Li, J. Wan, L. Huang, Y. Zhang, G. Feng and J. Zhou, *Nat. Commun.*, 2017, **8**, 15630.
8 M. E. Roberts, D. R. Wheeler, B. B. Mckenzie and B. C. Bunker, *J. Mater. Chem.*, 2009, **19**, 6977.
9 G. A. Snook, P. Kao and A. S. Best, *J. Power Sources*, 2011, **196**, 1.
10 A. Balducci, R. Dugas, P. L. Taberna, P. Simon, D. Plée, M. Mastragostino and S. Passerini, *J. Power Sources*, 2007, **165**, 922.
11 D. P. Dubal, O. Ayyad, V. Ruiz and P. G. Romero, *Chem. Soc. Rev.*, 2015, **44**, 1777.
12 X. Peng, K. Huo, J. Fu, B. Gao, L. Wang, L. Hu, X. Zhang and P. K. Chu, *ChemElectroChem*, 2015, **2**, 512.
13 C. Zhu, P. Yang, D. Chao, X. Wang, X. Zhang, S. Chen, B. K. Tay, H. Huang, H. Zhang, W. Mai and H. Fan, *Adv. Mater.*, 2015, **27**, 4566.
14 G. Ma, Z. Wang, B. Gao, T. Ding, Q. Zhong, X. Peng, J. Su, B. Hu, L. Yuan, P. K. Chu, J. Zhou and K. Huo, *J. Mater. Chem. A*, 2015, **3**, 14617.
15 B. Gao, X. Li, X. Guo, X. Zhang, X. Peng, L. Wang, J. Fu, P. K. Chu and K. Huo, *Adv. Mater. Interfaces*, 2015, **2**, 1500211.
16 X. Xiao, H. Yu, H. Jin, M. Wu, Y. Fang, J. Sun, Z. Hu, T. Li, J. Wu, L. Huang, Y. Gogotsi and J. Zhou, *ACS Nano*, 2017, **11**, 2180.
17 C. Huang, Y. Yang, J. Fu, J. Wu, H. Song, X. Zhang, B. Gao, P. K. Chu and K. Huo, *J. Nanosci. Nanotechnol.*, 2017, **18**, 30.
18 H. Cui, G. Zhu, X. Liu, F. Liu, Y. Xie, C. Yang, T. Lin, H. Gu and F. Huang, *Adv. Sci.*, 2015, **2**, 1500126.
19 X. Wu, Q. Wang, W. Zhang, Y. Wang and W. Chen, *Ceram. Int.*, 2016, **42**, 15077.
20 M. Liu, T. Yang, J. Chen, L. Su, K. C. Chou and X. Hou, *J. Alloys Compd.*, 2016, **692**, 605.
21 X. Peng, K. Huo, J. Fu, X. Zhang, B. Gao and P. K. Chu, *Chem. Commun.*, 2013, **49**, 10172.
22 H. Pang, S. J. Ee, Y. Dong, X. Dong and P. Chen, *ChemElectroChem*, 2014, **1**, 1027.
23 D. Choi and P. N. Kumta, *J. Electrochem. Soc.*, 2006, **153**, A2298.
24 D. J. Kim, J. K. Kim, J. H. Lee, H. H. Cho, Y. S. Bae and J. H. Kim, *J. Mater. Chem. A*, 2016, **4**, 12497.
25 K. Huo, X. Li, B. Gao, L. Wang, Q. Li, X. Peng, X. Zhang, J. Fu and P. K. Chu, *ChemElectroChem*, 2016, **3** 1301.
26 B. L. Ellis, P. Knauth and T. Djenizian, *Adv. Mater.*, 2014, **26**, 3368.
27 P. Yang, D. Chao, C. Zhu, X. Xia, Y. Zhang, X. Wang, P. Sun, B. K. Tay, Z. X. Shen, W. Mai and H. J. Fan, *Adv. Sci.*, 2016, **3**, 1500299.
28 X. Lu, G. Wang, T. Zhai, M. Yu, S. Xie, Y. Ling, C. Liang, Y. Tong and Y. Li, *Nano Lett.*, 2012, **12**, 5376.
29 Y. Xie, C. Xia, H. Du and W. Wang, *J. Power Sources*, 2015, **286**, 561.
30 Z. Peng, J. Lin, R. Ye, E. L. G. Samuel and J. M. Tour, *ACS Appl. Mater. Interfaces*, 2015, **7**, 3414.
31 P. Sun, R. Lin, Z. Wang, M. Qiu, Z. Chai, B. Zhang, H. Meng, S. Tan, C. Zhao and W. Mai, *Nano Energy*, 2017, **31**, 432.
32 M. F. E. Kady and R. B. Kaner, *Nat. Commun.*, 2013, **4**, 1475.
33 P. Pande, P. G. Rasmussen and L. T. Thompson, *J. Power Sources*, 2012, **207**, 212.
34 Z. H. Huang, T. Y. Liu, Y. Song, Y. Li and X. X. Liu, *Nanoscale*, 2017, **9**, 13119.

35 C. Deng, F. Ding, X. Li, Y. Guo, W. Ni, H. Yan, K. Sun and Y. M. Yan, *J. Mater. Chem. A*, 2015, **4**, 59.
36 L. N. Zhang, S. Li, H. Q. Tan, S. U. Khan, Y. Y. Ma, H. Y. Zang, Y. Wang and Y. G. Li, *ACS Appl. Mater. Interfaces*, 2017, **9**, 16270.
37 M. Kaempgen, C. K. Chan, J. Ma, Y. Cui and G. Gruner, *Nano Lett.*, 2009, **9**, 1872.
38 H. Zheng, T. Zhai, M. Yu, S. Xie, C. Liang, W. Zhao, S. C. I. Wang, Z. Zhang and X. Lu, *J. Mater. Chem. C*, 2013, **1**, 225.
39 Z. Q. Hou, Z. Y. Wang, L. X. Yang and Z. G. Yang, *RSC Adv.*, 2017, **7**, 25732.
40 S. Wang, C. Sun, Y. Shao, Y. Wu, L. Zhang and X. Hao, *Small*, 2017, **13**, 1603330.
41 T. Zhai, X. Lu, Y. Ling, M. Yu, G. Wang, T. Liu, C. Liang, Y. Tong and Y. Li, *Adv. Mater.*, 2014, **26**, 5869.
42 P. Yang, X. Xiao, Y. Li, Y. Ding, P. Qiang, X. Tan, W. Mai, Z. Lin, W. Wu, T. Li, H. Jin, P. Liu, J. Zhou, C. P. Wong and Z. L. Wang, *ACS Nano*, 2013, **7**, 2617.
43 Z. Peng, R. Ye, J. A. Mann, D. Zakhidov, Y. Li, P. R. Smalley, J. Lin and J. M. Tour, *ACS Nano*, 2015, **9**, 5868.
44 Z. Wang, Z. Zhu, J. Qiu and S. Yang, *J. Mater. Chem. C*, 2014, **2**, 1331.
45 R. Wang, C. Xia, N. Wei and H. N. Alshareef, *Electrochim. Acta*, 2016, **196**, 611.
46 V. T. Le, H. Kim, A. Ghosh, J. Kim, J. Chang, Q. A. Vu, D. T. Pham, J. H. Lee, S. W. Kim and Y. H. Lee, *ACS Nano*, 2013, **7**, 5940.

Supporting Information

Hierarchical TiN Nanoparticles Assembled Nanopillars for Flexible Supercapacitors with High Volumetric Capacitance

Ping Qin,[a†] Xingxing Li,[a†] Biao Gao,[a*] Jijiang Fu,[a] Lu Xia,[a] Xuming Zhang,[a*] Kaifu Huo,[b] Wenli Shen[c] and Paul K. Chu[d]

[a] The State Key Laboratory of Refractories and Metallurgy, Institute of Advanced Materials and Nanotechnology, Wuhan University of Science and Technology, Wuhan 430081, China.

[b] Wuhan National Laboratory for Optoelectronics (WNLO), School of Optical and Electronic Information Huazhong University of Science and Technology Wuhan 430074, China.

[c] Department of Physics, Arizona state University, Tempe 85281, USA.

[d] Department of Physics and Department of Materials Science and Engineering, City University of Hong Kong, Tat Chee Avenue, Kowloon, Hong Kong, China.

* Corresponding author:

E-mail: gaobiao@wust.edu.cn (B. Gao); xumzhang@wust.edu.cn (X. Zhang)

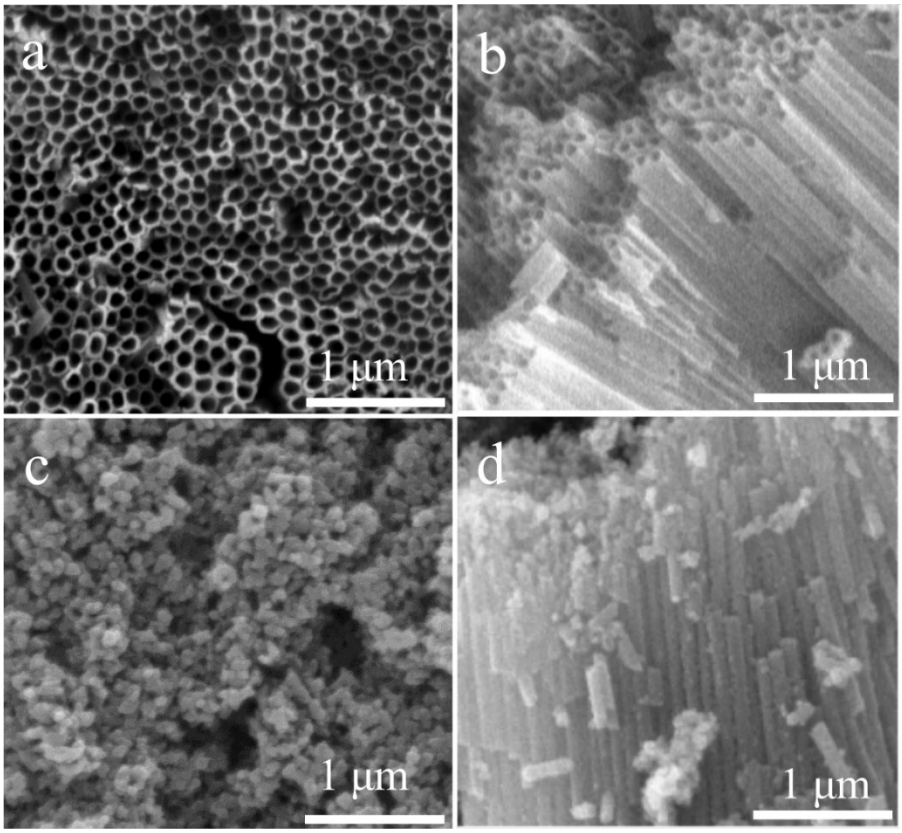

Fig. S1. (a) Top-view and (b) side-view SEM images of the TiO_2 NTs; (c) Top-view and (d) side-view SEM images of the H-TiO_2 NPs.

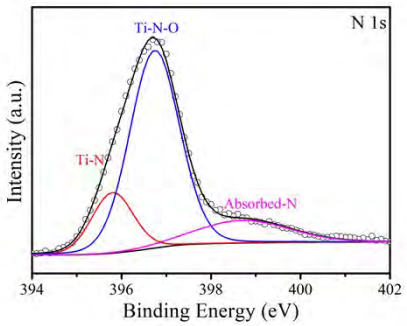

Fig. S2. XPS spectra of N 1s of the H-TiN NPs.

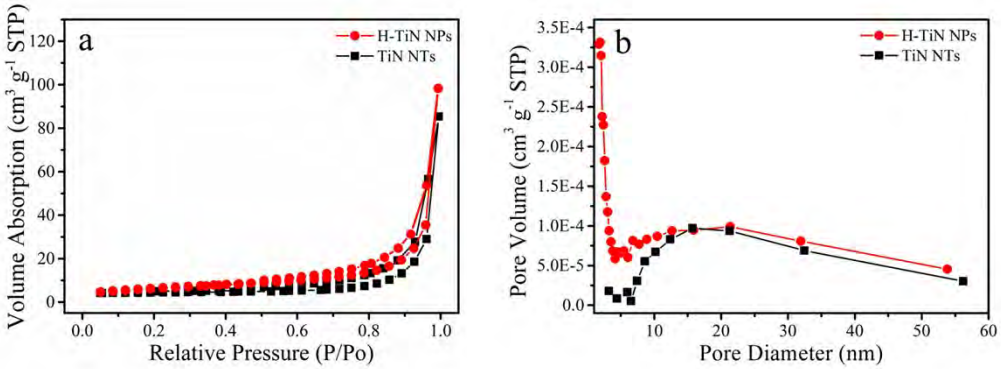

Fig. S3. (a) N_2 adsorption-desorption isotherms and (b) the pore size distribution of the H-TiN NPs and TiN NTs.

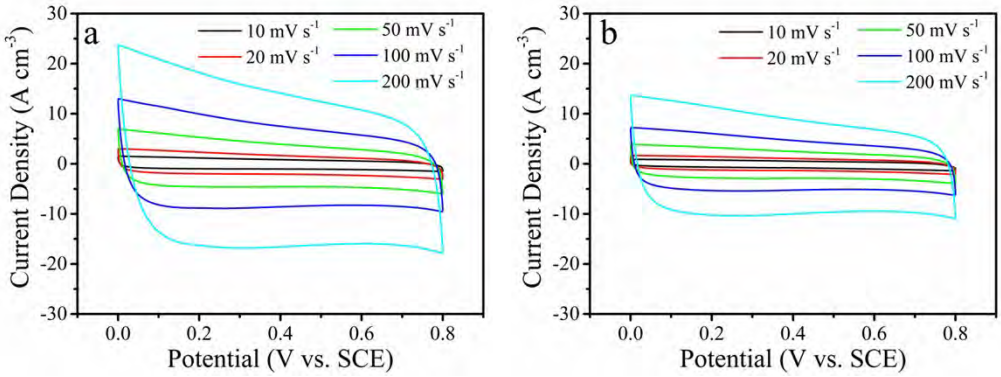

Fig. S4. CV curves of (a) H-TiN NPs and (b) TiN NTs at different scanning rates from 10 to 200 mV s^{-1}.

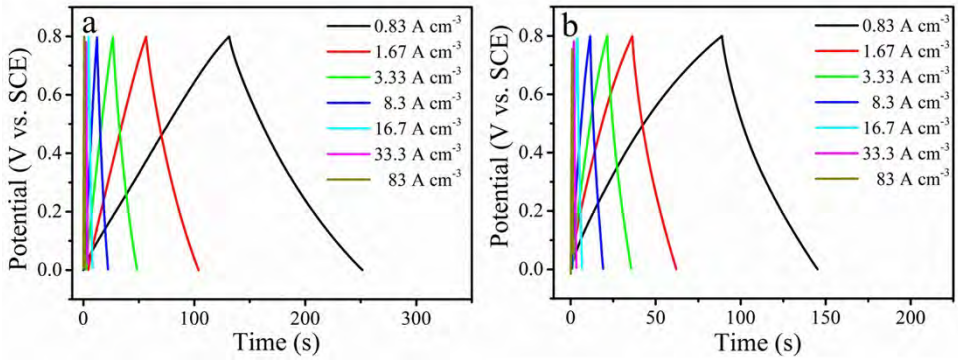

Fig. S5. GCD curves of the (a) H-TiN NPs and (b) TiN NTs at different current densities from 0.83 to 83 A cm^{-3} in 1 M H_2SO_4.

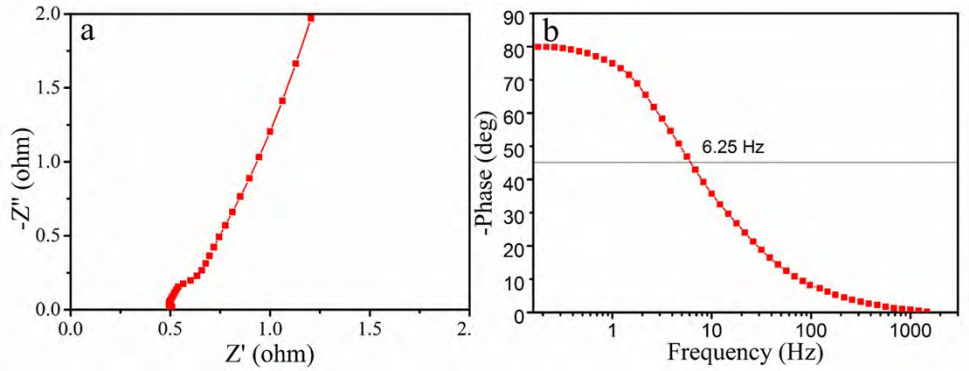

Fig. S6. (a) The electrochemical impedance spectroscopy and (b) the characteristic frequency for a phase angle marks at -45^{o} point of the H-TiN NPs.

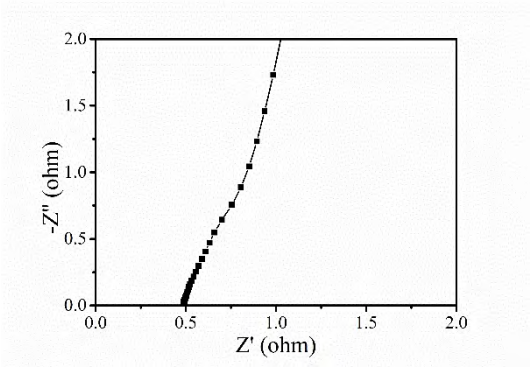

Fig. S7. The electrochemical impedance spectroscopy of the TiN NTs.

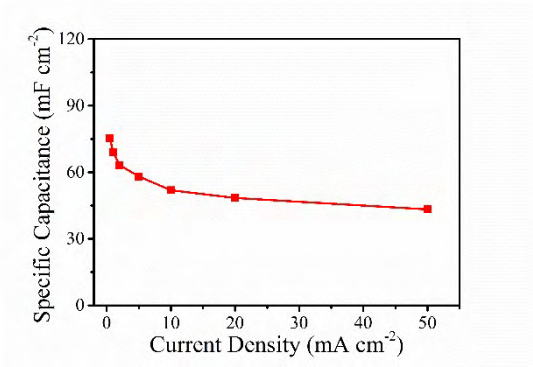

Fig. S8. The areal specific capacitances of H-TiN NPs at different current densities.

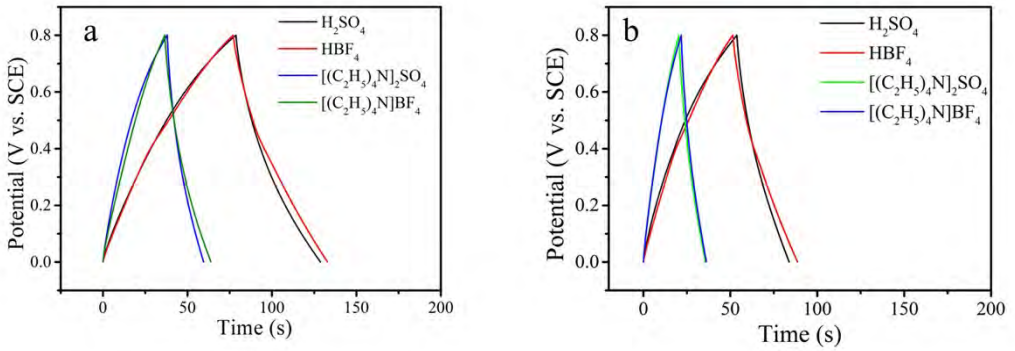

Fig. S9. GCD curves of (a) H-TiN NPs and (b) TiN NTs at a current density of 0.83 A cm^{-3} in 0.1 M H_2SO_4, 0.1 M HBF_4, 0.1 M $[(C_2H_5)_4N]_2SO_4$ and 0.1 M $[(C_2H_5)_4N]BF_4$.

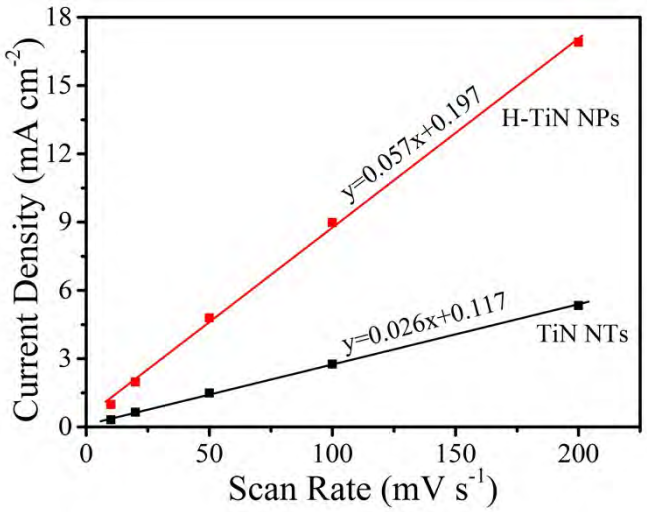

Fig. S10. The relationship of scan rate and current density of H-TiN NPs and TiN NTs collecting from CV curves at a potential of 0.4 V. The slope value represents the effective active surface area.

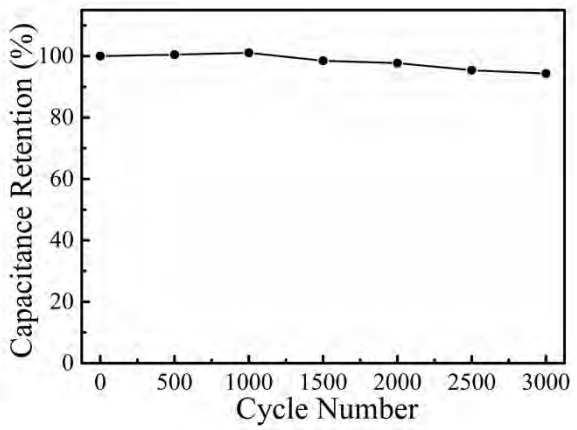

Fig. S11. Cycling stability of the H-TiN NPs electrode measured by CV at a scanning rate of 200 mV s^{-1}.